High frequency magnetic fluctuations correlated with the inter-ELM pedestal evolution in ASDEX Upgrade

F. M. Laggner[1], E. Wolfrum[2], M. Cavedon[2,3], F. Mink[2,3], E. Viezzer[2], M. G. Dunne[2], P. Manz[2,3], H. Doerk[2], G. Birkenmeier[2,3], R. Fischer[2], S. Fietz[2], M. Maraschek[2], M. Willensdorfer[2], F. Aumayr[1], the EUROfusion MST1 Team* and the ASDEX Upgrade Team

[1] Institute of Applied Physics, TU Wien, Fusion@ÖAW, Wiedner Hauptstr. 8-10, 1040 Vienna, Austria

[2] Max Planck Institute for Plasma Physics, Boltzmannstr. 2, 85748 Garching, Germany

[3] Physik-Department E28, Technische Universität München, James-Franck-Str.1, 85748 Garching, Germany

* See http://www.euro-fusionscipub.org/mst1.

E-mail: laggner@iap.tuwien.ac.at

Abstract.

In order to understand the mechanisms that determine the structure of the high confinement mode (H-mode) pedestal, the evolution of the plasma edge electron density and temperature profiles between edge localised modes (ELMs) is investigated. The onset of radial magnetic fluctuations with frequencies above 200 kHz is found to correlate with the stagnation of the electron temperature pedestal gradient. During the presence of these magnetic fluctuations the gradients of the edge electron density and temperature are clamped and stable against the ELM onset. The detected magnetic fluctuation frequency is analysed for a variety of plasma discharges with different electron pressure pedestals. It is shown that the magnetic fluctuation frequency scales with the neoclassically estimated $E \times B$ velocity at the plasma edge. This points to a location of the underlying instability in the gradient region. Furthermore, the magnetic signature of these fluctuations indicates a global mode structure with toroidal mode numbers of approximately 10. The fluctuations are also observed on the high field side with significant amplitude, indicating a mode structure that is symmetric on the low field side and high field side. The associated fluctuations in the current on the high field side might be attributed to either a strong peeling part or the presence of non-adiabatic electron response.

Keywords: plasma, tokamak, H-mode, edge localised modes, profile

1. Introduction

In the high confinement mode (H-mode) the particle and energy transport in the edge region of a toroidally confined plasma is reduced by an edge transport barrier (ETB) [1]. The ETB provokes steep gradients in the edge density and temperature profiles, called a pedestal. Profile stiffness [2] transfers the increased pressure from the edge directly to the core plasma. The pedestal, therefore, strongly impacts the performance of fusion plasmas. However, in most operational conditions, the pedestal is generally not temporally stable because the steep gradients are limited by the occurrence of quasi-periodic edge instabilities, better known as edge localised modes (ELMs) [3]. Since ELMs cause large particle and heat fluxes towards the wall [4], they have been in the focus of research for several years [5].

The widely accepted theory to explain the stability limit of the pedestal is the peeling-ballooning theory [6]. It couples pressure gradient driven (ballooning) and current gradient driven (peeling) modes to determine the pedestal stability limit. To predict the pedestal shape (height and width) of a fusion plasma, an additional constraint is required. Here, e.g. the EPED model [7] assumes the onset of kinetic ballooning modes (KBMs), limiting the maximum achievable pressure gradient before the ELM crash. Furthermore, simulations using different gyrokinetic codes show that the pre-ELM pedestal is unstable to several microinstabilities, the most prominent being microtearing modes (MTMs) and KBMs. This modelling predicts that MTMs exist at the pedestal top of MAST [8, 9], JET [10] and ASDEX Upgrade [11, 12], where also experimental evidence of MTMs has been found [13]. In several machines KBMs are shown to be unstable at least in parts close to the extreme edge of the steep gradient region [14, 10, 15].

Previous experimental investigations of the inter-ELM profile evolution [16] revealed that the fully developed gradients of density and temperature prior to the ELM onset stay almost constant for a period of the order of milliseconds. Additionally, several observations from different experiments (ASDEX Upgrade [17], Alcator C-Mod [18, 19] and DIII-D [20]) report the onset of high frequency magnetic fluctuations ($f > 150\,\mathrm{kHz}$) that originate from the plasma edge region. Therefore, they are very likely connected to the pedestal evolution in between ELMs. The underlying instabilities causing these fluctuations could possibly be the reason for the limitation of the pedestal gradients prior to the ELM onset.

The presented work characterises these high frequency magnetic fluctuations and relates them to pedestal parameters to gain deeper insight into the underlying processes and driving instabilities. Section 2 introduces the methods used to evaluate the plasma edge electron density (n_e) and electron temperature (T_e) profiles using the integrated data analysis (IDA) framework [21] at ASDEX Upgrade. In the following (section 3) two representative discharges with similar ratio of electron to magnetic pressure (β_e), in which high frequency magnetic fluctuations prior to the ELM occur, are exemplarily presented. Their onset is then related to the pedestal profile evolution. Additionally,

using a larger set of data the fluctuation frequency is related to the plasma edge poloidal rotation. In section 4 the fluctuations are shown to be also observable on the high field side (HFS) and the toroidal mode numbers (n), determined from the magnetic signals, are presented. Finally, an estimation of the magnetic fluctuation location using the detected fluctuation frequency and the background E × B velocity is presented. An interpretation of the observations is given in section 5, that indicates non-thermal electron response or strong peeling drive causing a saturated mode in the pedestal.

2. Pedestal profile analysis

To investigate the inter-ELM pedestal profile evolution, plasma diagnostics with high spatial and temporal resolution are required to resolve full subsequent ELM cycles. The IDA framework [21] at ASDEX Upgrade provides the capability to combine the information from different plasma diagnostics within Bayesian probability theory (BPT) to evaluate the best fits of n_e and T_e (parameterised by cubic splines). For the presented n_e profiles, the information from lithium beam emission spectroscopy (Li-BES) [22, 23, 24] for the edge density and deuterium cyanide laser interferometry (DCN) [25] for the core density is combined. The T_e profiles are reconstructed from electron cyclotron emission (ECE) [26] using the electron cyclotron forward modelling (ECFM) [27]. The ECFM models the ECE propagation in both optically thick and optically thin plasmas. To fit the ECE 'shine-through' at the plasma edge, the alignment of the density and temperature profile is crucial. For this reason, the profiles are aligned relative to the profiles of the Thomson scattering (TS) diagnostic [28], that measures n_e and T_e simultaneously at identical positions. Here, the T_e is slightly shifted ($< 3\,\mathrm{mm}$) that 100 eV at the separatrix is achieved [29, 30]. The presented profiles in this work are analysed with a temporal resolution of 250 μs, which is sufficient to resolve the full ELM cycle (duration 10 ms) and long enough to suppress noise induced scattering of the profiles.

Using the ECFM the T_e profiles as well as the T_e gradients can be reliably evaluated all the way to the separatrix; this is essential in the presented work because the onset of the high frequency magnetic fluctuations is correlated to the inter-ELM recovery of maximum electron temperature gradient ($\max(-\nabla T_\mathrm{e})$) at the edge. Figure 1 presents ELM synchronised profiles (averaged between −2 and −1 ms relative to the ELM onset) for n_e (a), T_e (b) and β_e (c). Two discharges with different pedestal top electron collisionality ($\nu^*_\mathrm{e,ped}$) (high $\nu^*_\mathrm{e,ped} \approx 1.5$, #30701, blue; low $\nu^*_\mathrm{e,ped} \approx 0.6$, #30721, red) and almost identical pedestal β_e are compared. The β_e profile is calculated with

$$\beta_\mathrm{e} = \frac{n_\mathrm{e} T_\mathrm{e}}{B^2/2\mu_0} \tag{1}$$

using the local magnetic field (B) at the low field side (LFS) midplane and the vacuum permeability (μ_0). The approximation of the electron collisionality (ν^*_e) given

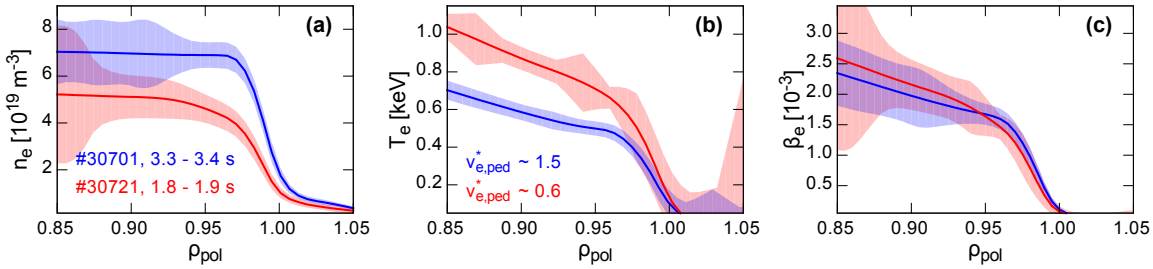

Figure 1: Pre-ELM (averaged between −2 and −1 ms relative to the ELM onset) profiles of (a) n_e, (b) T_e and (c) β_e. The shaded areas represent the propagated variation of the uncertainties in the data evaluation (IDA) and the standard deviation of the ELM synchronised average. Both discharges have similar β_e profiles and vary in $\nu^*_{e,ped}$.

in reference [31], is modified by approximating the Coulomb logarithm leading to

$$\nu^*_{e,ped} = 0.0012 \frac{q R_0 Z_{eff} n_e[10^{19}\,\mathrm{m}^{-3}]}{\epsilon^{3/2}(T_e[\mathrm{keV}])^2}, \tag{2}$$

which is locally evaluated at the pedestal top ($\rho_{pol} = 0.96$) using the major plasma radius (R_0), the safety factor (q), the effective charge (Z_{eff}) and the inverse aspect ratio (ϵ). Here, Z_{eff} is set to 1 because there is no accurate measurement and the discharge conditions in both presented plasmas were similar.

Both discharges were performed at a plasma current (I_p) 1.0 MA, toroidal magnetic field (B_t) −2.5 T (negative sign stands for opposite direction to I_p) and identical plasma shape. The variation of $\nu^*_{e,ped}$, simultaneously keeping β_e constant, was achieved by a variation of heating power (P_{heat}) and externally applied gas puff. In the high $\nu^*_{e,ped}$ case, P_{heat} (from neutral beam injection (NBI) and electron cyclotron resonance heating (ECRH)) was 5.3 MW and the external deuterium puff was $11.3 \cdot 10^{21}$ e/s. Compared to this in the low $\nu^*_{e,ped}$ case P_{heat} was increased to 6.9 MW and the gas puff decreased to $2.1 \cdot 10^{21}$ e/s. In the following these discharges will be compared in terms of inter-ELM pedestal evolution and the onset of high frequency magnetic fluctuations will be characterised.

3. Pedestal profile evolution and onset of magnetic fluctuations

To detect radial magnetic field fluctuations ($\partial B_r/\partial t$), several ballooning coils are installed in ASDEX Upgrade. For the presented investigation, a coil located at the LFS midplane (B31-14) was used (c.f. section 4, figure 5). Figure 2a presents a spectrogram of $\partial B_r/\partial t$ in the top plot. Additionally, time traces of n_e (blue), T_e (red) at the pedestal top ($\rho_{pol} = 0.96$) and inner divertor current (black) are shown. The grey shaded area indicates a period when the Li-Beam was modulated to subtract the background emission [32]. In this time interval no n_e profiles are available and therefore, ECFM is not possible and T_e profiles are not evaluated.

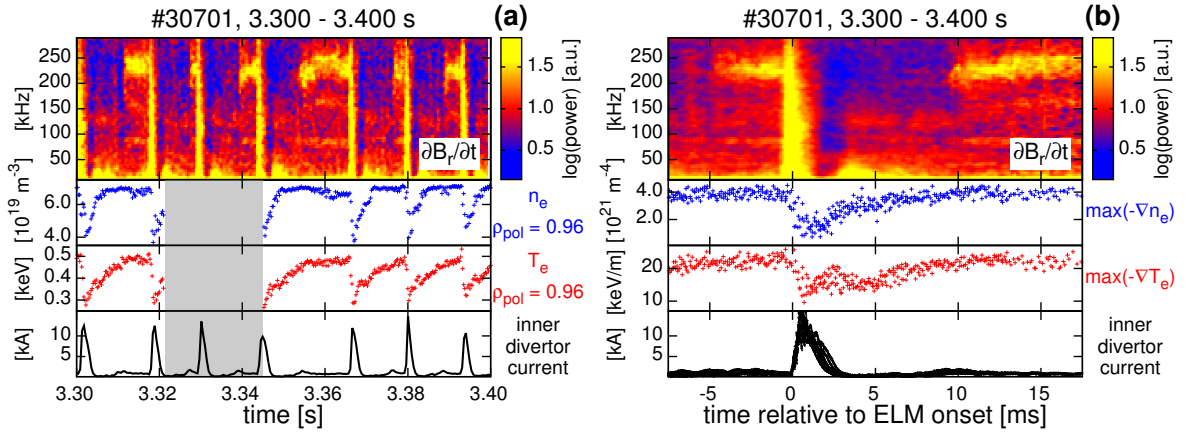

Figure 2: Pedestal evolution of the high $\nu^*_{\mathrm{e,ped}}$ case (#30701): (a) Spectrogram of $\partial B_\mathrm{r}/\partial t$ (top) and time traces of n_e (blue), T_e (red) at the pedestal top ($\rho_\mathrm{pol} = 0.96$) and inner divertor current (black). The grey shaded area indicates when the Li-beam was switched off. (b) ELM-synchronised spectrogram of $\partial B_\mathrm{r}/\partial t$ and ELM-synchronised time traces of $\max(-\nabla n_\mathrm{e})$ (blue), $\max(-\nabla T_\mathrm{e})$ (red) and inner divertor current (black). After $\max(-\nabla T_\mathrm{e})$ is recovered (10 ms after the ELM onset) fluctuations with a frequency of approximately 240 kHz set in.

The pulse of the divertor current (black) indicates the ELM. Although the ELM frequency varies slightly, the pedestal recovery is very similar for each ELM until the pre-ELM temperature gradient (directly related to the pre-ELM pressure gradient) is reached. This can be seen in figure 2b, where an ELM synchronised spectrogram of $\partial B_\mathrm{r}/\partial t$ is presented together with $\max(-\nabla n_\mathrm{e})$ (blue), $\max(-\nabla T_\mathrm{e})$ (red) and inner divertor current (black). ELM synchronised plots superimpose the datapoints (for spectrograms the windows of the Fourier transform) with respect to the ELM onset. The first recovery phase of $\max(-\nabla n_\mathrm{e})$, in which also the pedestal top n_e is re-established (5 ms after the ELM onset), appears before the $\max(-\nabla T_\mathrm{e})$ recovery. This is in agreement with previous observations [16]. Correlated to the recovery of $\max(-\nabla n_\mathrm{e})$ the onset of magnetic fluctuations in the region of up to 150 kHz is observed (4 ms after the ELM onset). These fluctuations are then present throughout the ELM cycle and in section 4 they will be related to low toroidal mode numbers (n). When the $\max(-\nabla T_\mathrm{e})$ is re-established (10 ms after the ELM onset) magnetic fluctuations with rather high frequencies (240 kHz) start. These fluctuations continue till the next ELM crash, which occurs between 10 and 17 ms after the previous ELM. In this phase, i.e. from approximately 10 ms after the ELM only data up to 1.5 ms before the following ELM are plotted in figure 2b. Only marginal changes in $\max(-\nabla n_\mathrm{e})$ and $\max(-\nabla T_\mathrm{e})$ can be seen during this period. The next ELM crash interrupts the fluctuations, which set in again after the recovery of $\max(-\nabla n_\mathrm{e})$ and $\max(-\nabla T_\mathrm{e})$. This behaviour can also be seen in figure 2a in the evolution of the pedestal top T_e (red points). The onset of the high frequency fluctuations is clearly correlated with the recovery of the

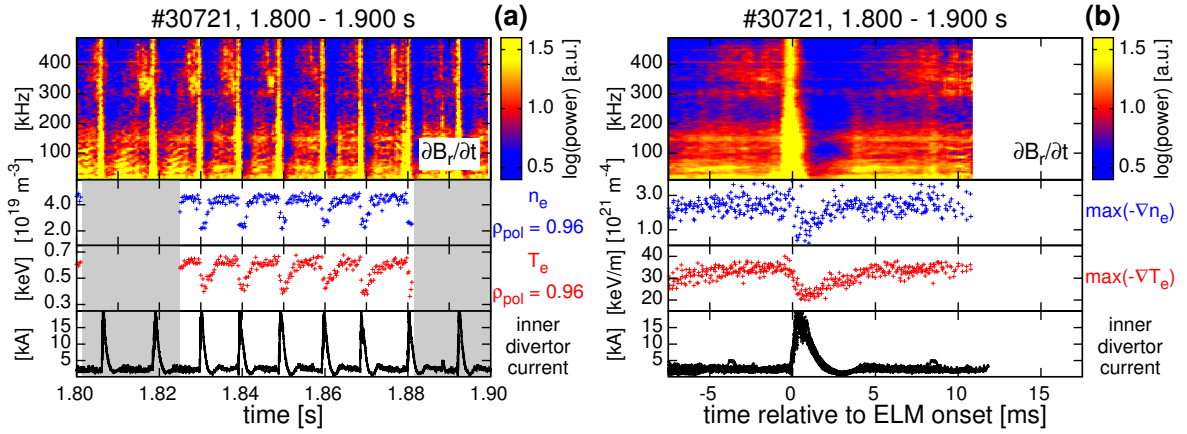

Figure 3: Pedestal evolution of the low $\nu^*_{\mathrm{e,ped}}$ case (#30721): (a) Spectrogram of $\partial B_\mathrm{r}/\partial t$ (top) and time traces of n_e (blue), T_e (red) at the pedestal top ($\rho_\mathrm{pol} = 0.96$) and inner divertor current (black). (b) ELM-synchronised spectrogram of $\partial B_\mathrm{r}/\partial t$ and ELM-synchronised time traces of $\max(-\nabla n_\mathrm{e})$ (blue), $\max(-\nabla T_\mathrm{e})$ (red) and inner divertor current (black). Identical observations as in the high $\nu^*_{\mathrm{e,ped}}$ case can be made: The onset of high frequency magnetic fluctuations occurs after the recovery of the $\max(-\nabla T_\mathrm{e})$.

T_e pedestal and, consequently, the electron pressure (p_e) pedestal (since the n_e pedestal recovers before). However, the duration of the high frequency fluctuations (with almost unchanged pedestal gradients) slightly differs in the presented case from ELM to ELM (figure 2a). This indicates that the observed fluctuations are not ELM-precursors in a classical sense, since for ELM-precursors one would expect a continuous growth in amplitude leading to the ELM crash and therefore, similar duration before the ELM onset. While the high frequency fluctuation is present, no clear change in the fluctuation amplitude (growth) can be seen. This observation is better explained by a saturated mode that onsets when a certain threshold (in terms of pedestal parameters) is exceeded. The mode is then affected either by the ELM crash itself, or the ELM-induced flattening of the pedestal leads to the vanishing of the drive.

In the low $\nu^*_{\mathrm{e,ped}}$ discharge a similar behaviour of the inter-ELM pedestal profile evolution is observed (figure 3, same setup as figure 2). The recovery of $\max(-\nabla n_\mathrm{e})$ and $\max(-\nabla T_\mathrm{e})$ shows identical behaviour as in the high $\nu^*_{\mathrm{e,ped}}$ case (figure 2b). The ELM frequency is larger than in the high $\nu^*_{\mathrm{e,ped}}$ case since P_heat is higher. When $\max(-\nabla T_\mathrm{e})$ is re-established (6 ms after the ELM onset), broadband fluctuations also set in, in this case with a frequency between 300 and 400 kHz set in. The frequency bandwidth is larger than in the high $\nu^*_{\mathrm{e,ped}}$ case and the fluctuations are not clearly and intensely seen for every ELM crash (figure 3a). Important to note here is that the fluctuation frequency strongly differs from the one observed in the high $\nu^*_{\mathrm{e,ped}}$ case. Nevertheless, the onset of the fluctuations is again correlated with the pedestal pressure (temperature) recovery pointing into the direction that the detected high frequency fluctuations (at low and high $\nu^*_{\mathrm{e,ped}}$) have the same origin.

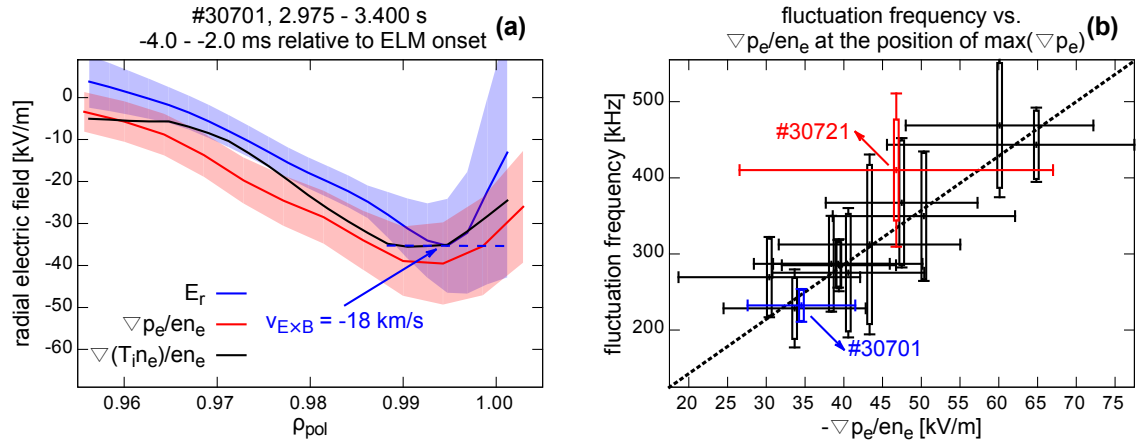

Figure 4: E_r, $\nabla p_\mathrm{e}/en_\mathrm{e}$ and fluctuation frequency: (a) Example profile of E_r (the blue dashed line indicates a $v_{\mathrm{E}\times\mathrm{B}}$ of $-18\,\mathrm{km/s}$) and (b) $\partial B_\mathrm{r}/\partial t$ frequency over $-\nabla p_\mathrm{e}/en_\mathrm{e}$ ($\propto -E_\mathrm{r}$). The boxes along the frequency axis indicate the width of the fluctuation frequency band which can span up to 100 kHz. A linear dependence between the detected fluctuation frequency and the background flow velocity ($v_{\mathrm{E}\times\mathrm{B}}$) can be seen (dashed line).

Since the inter-ELM magnetic fluctuations occur in several plasma scenarios at different frequencies the pedestal profiles of several discharges are analysed and the detected fluctuation frequency is correlated with them. To explain the measured frequencies, it was assumed that the instabilities causing these fluctuations are located in the pedestal region [17, 18], because they are terminated by the ELM crash. In the pedestal region there is a strong background ($\mathbf{E}\times\mathbf{B}$) flow [33], mainly caused by the radial electric field (E_r). In H-mode, E_r at the plasma edge can be described by neoclassical theory [34]. For low toroidal rotation velocities the dominating term in E_r is $\nabla p_\mathrm{i}/en_\mathrm{i}$ (using main ion pressure (p_i) and main ion density (n_i)).

Since no measurements in the required temporal resolution were available for n_i and ion temperature (T_i), the quantities entering $\nabla p_\mathrm{i}/en_\mathrm{i}$ are approximated by $\nabla n_\mathrm{i}/n_\mathrm{i} \approx \nabla n_\mathrm{e}/n_\mathrm{e}$ and $\max(\nabla T_\mathrm{i}) \approx \max(\nabla T_\mathrm{e})$. This should be valid in the plasma steep gradient region, especially in highly collisional plasmas. An example profile of E_r (red), evaluated by charge exchange recombination spectroscopy (CXRS) [35], is compared to the estimations of $\nabla(T_\mathrm{i}n_\mathrm{e})/en_\mathrm{e}$ (black) and $\nabla p_\mathrm{e}/en_\mathrm{e}$ (blue) in figure 4a. The profiles agree within their errorbars and have their minimum at $-35\,\mathrm{kV/m}$, which corresponds to a $v_{\mathrm{E}\times\mathrm{B}}$ of $-18\,\mathrm{km/s}$ (the negative sign indicates propagation into the electron diamagnetic direction). $\nabla(T_\mathrm{i}n_\mathrm{e})/en_\mathrm{e}$ and $\nabla p_\mathrm{e}/en_\mathrm{e}$ have similar shapes (within the uncertainties) justifying the approximation of $\nabla p_\mathrm{i}/en_\mathrm{i}$ by $\nabla p_\mathrm{e}/en_\mathrm{e}$.

Figure 4b presents the fluctuation frequency (considering only frequency bands at a statistical distribution $> 200\,\mathrm{kHz}$) with respect to $-\nabla p_\mathrm{e}/en_\mathrm{e}$, taken at the position of the maximum electron pressure gradient ($\max(\nabla p_\mathrm{e})$) (averaged between -2.0 and $-0.5\,\mathrm{ms}$ relative to the ELM onset), for a set of 12 discharge intervals. The boxes on the frequency axis show the bandwidth of fluctuation, determined by a full width at

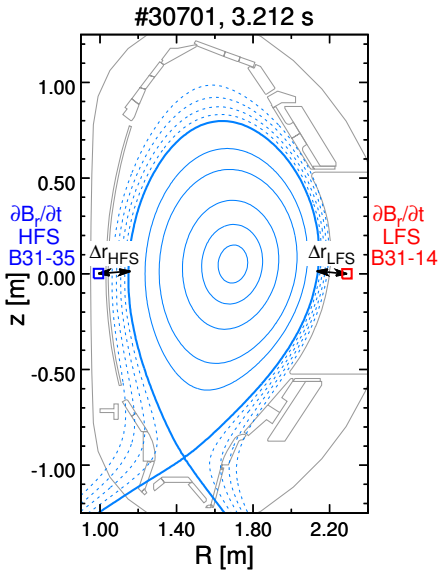

Figure 5: Ballooning coil positions: $\partial B_\mathrm{r}/\partial t$ is detected at the LFS as well as at the HFS midplane. The coils have different distances to the mode location (Δr). For $\rho_{pol} = 0.99$ (steep gradient region) the LFS coil is approximately 8 mm closer to the flux surface than the HFS coil.

half maximum (FWHM) criterion. The discharge intervals were chosen to span a wide range $-\nabla p_\mathrm{e}/en_\mathrm{e}$ and show the onset of magnetic fluctuations connected to the clamping of the pedestal gradients in the ELM cycle (c.f. section 3). The values of $\nu^*_{\mathrm{e,ped}}$ range from 0.55 to 1.80 (c.f. section 2). At ASDEX Upgrade it has been found for a similar range of $\nu^*_{\mathrm{e,ped}}$ the minimum of E_r agrees well with the approximation $\nabla p/en$ [36].

A clear linear correlation between fluctuation frequency and $-\nabla p_\mathrm{e}/en_\mathrm{e}$ is observed, suggesting that the average detected frequency (in the lab frame) is caused by the background E × B flow velocity in the edge. From this relation (dashed line) the m and n number can be estimated using the safety factor (q), the poloidal and toroidal plasma circumference (c.f. equations 5, 6, 7). The fit of the relation gives $m \approx -55$ and corresponding $n \approx -11$ (using $q \approx 5$), which is in good agreement with the mode numbers determined from toroidally distributed ballooning coils (see section 4).

It should be noted that the fluctuation frequency can change slightly for single ELMs (c.f. figure 3a). This means that the analysis of single ELMs might give smaller bandwidths and different fluctuation frequencies connected to slightly changing $\nabla p_\mathrm{e}/en_\mathrm{e}$. However, owing to the limited time resolution and the uncertainties in the determination of the pedestal profiles this analysis can not be performed.

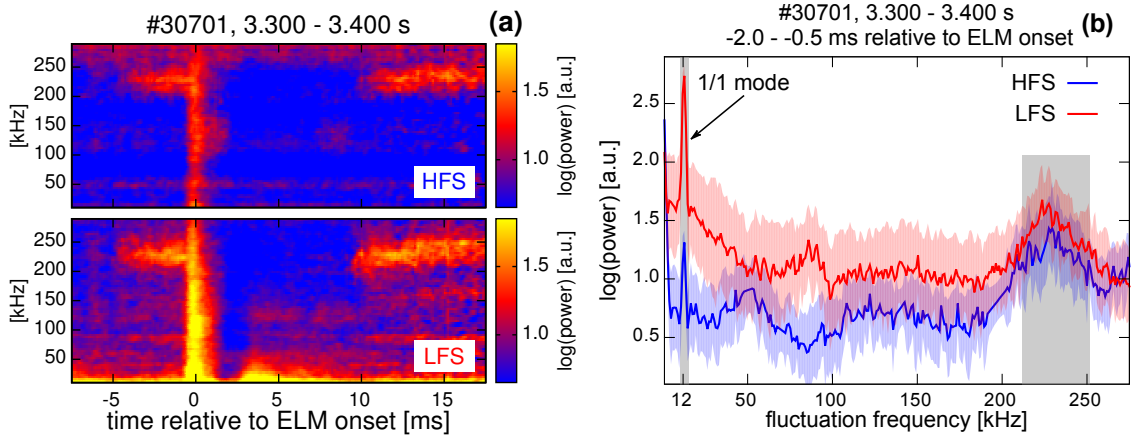

Figure 6: Comparison of the $\partial B_\mathrm{r}/\partial t$ intensity at LFS and HFS: (a) Spectrogram of the HFS (top) and the LFS ballooning coil signals, (b) Integrated spectrum before the ELM onset. The high frequency fluctuations (240 kHz) are also detected at the HFS although the coil sensitivity might be lower (c.f. 1/1 mode).

4. Mode detection on the HFS, toroidal mode numbers and estimation of the detected mode frequency

To characterise the structure of the observed inter-ELM magnetic fluctuations, ballooning coils at different poloidal locations can be used. In figure 5 the positions of two coils, located at the outboard (LFS, B31-14, red) and inboard (HFS, B31-35, blue) midplane, are indicated. Owing to the plasma position and shape, the HFS and LFS coil have different distances to the same flux surface and the magnetic axis (shown for $\rho_\mathrm{pol} = 0.99$). In cylindrical geometry with conducting wall the detected signal amplitude is lowered by $(r_\mathrm{m}/(r_\mathrm{m}+\Delta r))^{m+1}$ [37], using the distance between the geometric axis and the mode location (r_m), the distance between the mode location and the coil location (Δr) and the poloidal mode number (m). This effect has to be taken into account, if LFS and HFS amplitudes are compared to get further information on the observed fluctuations.

ELM-synchronised spectrograms of the LFS and HFS coil signals are presented in figure 6 (for the high $\nu^*_\mathrm{e,ped}$ case). Figure 6a shows the high frequency range for the spectrograms of the HFS (top) and LFS (bottom) coil. The inter-ELM fluctuation is clearly visible on the HFS too, appearing at similar time relative to the ELM onset as the fluctuations detected on the LFS. The strong HFS amplitude would not be expected if the fluctuations were caused by a ballooning type instability e.g. KBMs. In figure 6b the integrated spectrum from -2.5 to -0.5 ms relative to the ELM onset is shown. At 12 kHz a dominant mode is observable in both spectrograms, which is identified as $m/n = 1/1$ core mode. If one would assume the 1/1 mode amplitude does not change from LFS to HFS (neglecting $m \pm 1$ sidebands and their relative phase), then the lower spectral intensity, detected on the HFS might be attributed to the $(r_\mathrm{m}/(r_\mathrm{m} + \Delta r))^{m+1}$

decay. In cylindrical approximation the ratio of the detected LFS and HFS amplitudes for the 1/1 mode is given by

$$\left(\frac{r_\mathrm{m}/(r_\mathrm{m}+\Delta r_\mathrm{LFS})}{r_\mathrm{m}/(r_\mathrm{m}+\Delta r_\mathrm{HFS})}\right)^{1+1} = \left(\frac{r_\mathrm{m}+\Delta r_\mathrm{HFS}}{r_\mathrm{m}+\Delta r_\mathrm{LFS}}\right)^{1+1} \approx 1.38 \tag{3}$$

using $r_\mathrm{m} \approx 10.3\,\mathrm{cm}$, $\Delta r_\mathrm{HFS} \approx 60.0\,\mathrm{cm}$ and $\Delta r_\mathrm{LFS} \approx 49.6\,\mathrm{cm}$. However, this effect can only explain parts of the weaker HFS signal for the 1/1 mode. Since the HFS coil is located behind a tile of the inner heat shield, electromagnetic shielding might be one reason for the weaker detected signal. Additional causes might be different gain factors in the data acquisition (DAQ), although both coils use identical DAQ systems, or the inaccurate assumption of constant mode amplitude on LFS and HFS.

For the inter-ELM high frequency fluctuations the LFS to HFS ratio of the detectable amplitudes in cylindrical approximation is

$$\left(\frac{r_\mathrm{m}+\Delta r_\mathrm{HFS}}{r_\mathrm{m}+\Delta r_\mathrm{LFS}}\right)^{55+1} \approx 2.01 \tag{4}$$

using $r_\mathrm{m} \approx 48.9\,\mathrm{cm}$, $\Delta r_\mathrm{HFS} \approx 16.7\,\mathrm{cm}$ and $\Delta r_\mathrm{LFS} \approx 15.9\,\mathrm{cm}$ and $m \approx 55$. This would mean that the fluctuation amplitude on the HFS might be higher than detected, which is an indication that ballooning type instabilities may not be the cause of the high frequency fluctuations.

From a set of toroidally distributed LFS ballooning coils, the toroidal mode number (n) of the fluctuations can be determined. Since the signal response of the coils is frequency dependent, phase shifts between the coils are possible, leading to inaccurate fits of the mode numbers. To reduce the systematic errors, the transfer functions of the individual coils were measured and taken into account [38]. In figure 7 the n value distributions for the high $\nu^*_\mathrm{e,ped}$ case (a) and the low $\nu^*_\mathrm{e,ped}$ case (b) are presented. The n numbers are fitted in a time interval relative to the ELM onset and then superimposed for all ELMs occurring in the analysed discharge interval. The different time intervals relative to the ELM onset for both presented cases (high $\nu^*_\mathrm{e,ped}$ case: -2.5 and $-0.5\,\mathrm{ms}$ relative to the ELM onset; low $\nu^*_\mathrm{e,ped}$ case: -2.5 and $-1.0\,\mathrm{ms}$ relative to the ELM onset) are chosen since the high frequency fluctuations are dominantly present in different time windows relative to the ELM (compare figures 2b and 3b). In both cases in the frequency range up to 180 kHz clear mode numbers from $n = -2$ to $n = -8$ (negative sign for counter-current or electron diamagnetic rotation in the lab frame) are observed. These modes were previously called washboard modes [39]. Additionally, the onset of these washboard (150 kHz) modes is earlier in the ELM cycle and more connected to the recovery of the pedestal density (c.f. figure 2b). For the inter-ELM magnetic fluctuations with frequencies of 240 kHz (high $\nu^*_\mathrm{e,ped}$) and 375 kHz (low $\nu^*_\mathrm{e,ped}$) n is in the region of -10 to -12. In both cases there are artefacts from timepoints with ill defined mode numbers appearing around $n = 0$. The comparison of figure 7a and b shows that the observed fluctuations have a similar toroidal mode structure and the different detected frequencies correspond to different background plasma rotation velocities. This is consistent with the linear dependence of the detected fluctuation

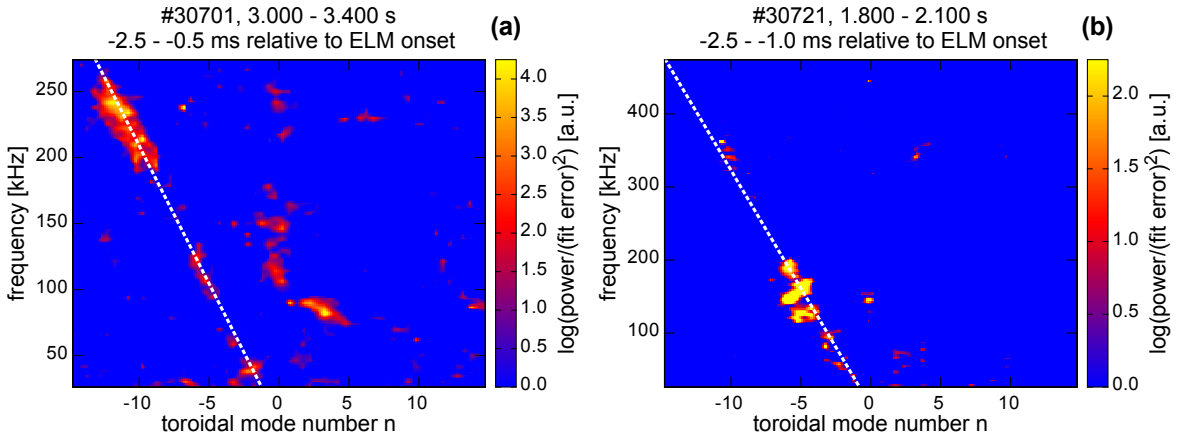

Figure 7: Toroidal mode number n distribution and corresponding frequencies: Determined from 5 toroidally distributed LFS midplane ballooning coils, (a) for the high $\nu^*_{\mathrm{e,ped}}$ and (b) low $\nu^*_{\mathrm{e,ped}}$ case. Positive values of n correspond to co-current rotation, negative n to counter-current (electron diamagnetic) rotation. The dashed white line indicates constant frequency over n (f/n) ratio and therefore, equal propagation velocity. The mode numbers of the high frequency fluctuations (at 240 kHz (a) and 375 kHz (b) are in both cases about -12.

frequency on $-\nabla p_\mathrm{e}/e n_\mathrm{e}$ found in section 3. Additionally, in both cases alignment (in terms of frequency over n, dashed white line in figure 7a, b) of the high frequency fluctuations and the low frequency washboard modes is found. This indicates that these modes have similar velocities (projected into the toroidal plane). If the contributions of toroidal and poloidal propagation in the projection are similar, low frequency washboard and high frequency fluctuations are situated at similar radial locations. However, it should be stated that just after the onset of the high frequency fluctuations a clamping of the pedestal $\max(-\nabla n_\mathrm{e})$ and $\max(-\nabla T_\mathrm{e})$ is observed.

The fact that the observed mode frequencies are proportional to $\nabla p_\mathrm{e}/e n_\mathrm{e}$, i.e. the minimum of E_r in the pedestal suggests that the modes are located in the steep gradient region of the pedestal. Using the evaluated $v_{\mathrm{E\times B}}$ and the observed mode number, one can try to estimate the detected fluctuation frequency in the lab frame and to compare this to the experimentally measured frequency. Figure 4a indicates the minimum of the measured $v_{\mathrm{E\times B}}$ velocity (blue dashed line), which is -18.0 ± 5.7 km/s for this case. At the position of the $v_{\mathrm{E\times B}}$ minimum, q is ≈ 5, the toroidal plasma circumference (U_tor) is 13.4 m, and the poloidal circumference (U_pol) is 3.9 m resulting in an average field line pitch angle (α)

$$\tan(\alpha) = \frac{1}{q} \cdot \frac{U_\mathrm{pol}}{U_\mathrm{tor}} \approx 0.05814. \tag{5}$$

Taking into account the 'barberpole effect', the projection of $v_{\mathrm{E\times B}}$ in the toroidal plane the total toroidal rotation observed in the lab frame ($v_{\mathrm{tor,lab}}$) is

$$v_{\mathrm{tor,lab}} = v_{\mathrm{E\times B}}/\sin(\alpha) + v_\mathrm{tor} \approx -299 \pm 88\,\mathrm{km/s} \tag{6}$$

with the toroidal plasma velocity ($v_{\mathrm{tor}} \approx 10\,\mathrm{km/s}$, measured by CXRS). The detected fluctuation frequency in the lab frame (f_{lab}) is given by

$$f_{\mathrm{lab}} = \frac{v_{\mathrm{tor,lab}} \cdot n}{U_{\mathrm{tor}}} \approx 268 \pm 78\,\mathrm{kHz} \tag{7}$$

using $n \approx -12$, which can be extracted from figure 7a for the magnetic fluctuation frequency of 240 kHz. This frequency agrees with the calculated f_{lab} within the experimental uncertainties, giving additional support to the hypothesis that the background plasma velocity dominates the mode propagation. Phase velocities of a few km/s in either direction cannot be extracted owing to the uncertainties of the background velocity.

5. Summary and discussion

For a variation of plasma edge density and temperature at ASDEX Upgrade it was found that the onset of high frequency fluctuations in the ELM cycle occurs at the same time as the re-establishment of the pedestal top pressure. During their presence, the maximum pressure gradient saturates meaning that the pre-ELM maximum pressure gradient is already achieved on the order of milliseconds before the ELM onset. The fluctuation frequency can be scaled with the neoclassical approximation of the radial electric field minimum, $\nabla p_{\mathrm{e}}/en_{\mathrm{e}}$, at the location of $\max(\nabla p_{\mathrm{e}})$. This indicates that the modes are localised in the steep gradient region and propagate with the background velocity. The uncertainties in the measurements of the background velocity profile do not allow the determination of the direction of phase velocities (electron or ion diamagnetic), if they are smaller than approximately 5 km/s.

The magnetic fluctuations show a strong signature also on the HFS. In the turbulence picture, the current fluctuations leading to $\partial B_{\mathrm{r}}/\partial t$ are in parallel direction to the magnetic field, which implicitly requires non-adiabatic electron response. This is possible in the plasma edge owing to the increasing field line connection length (increasing q), decreasing ion sound velocity (c_s) and steep gradients of the profiles [40, 41]. Consequently, the non-linear interaction between potential, pressure and current lead to magnetic fluctuations on the HFS, which do not necessarily have ballooning structure as an ideal linear MHD instability that is driven by the pedestal gradient on the LFS. The observed toroidal structure and the enhanced transport, leading to a clamping of the gradients, then might be the consequence of the interactions of potential, pressure and current fluctuations. Furthermore, the poloidal wave numbers ($k_\theta \rho_s$) $0.1 < k_\theta \rho_s < 0.2$ (calculated from the poloidal mode number), have similar scales at which KBMs and MTMs were found to be unstable in a comparable ASDEX Upgrade discharge [15].

On the other hand, in ELM-free regimes as quiescent H-mode (QH-mode) [42] or enhanced D_α (EDA) H-mode [43], modes at the very plasma edge were found, limiting the pressure gradient below the critical value. The magnetic signature of the EDA H-mode is rather broadband (between 0 and 200 kHz) and not comparable

to the fluctuations investigated here. For the QH-mode an edge harmonic oscillation (EHO) has been found, which usually has frequencies < 50 kHz. At ASDEX Upgrade additionally a high frequency oscillation (HFO) is present simultaneously to the EHO, which has frequencies in the range of 350 to 500 kHz [44, 45], which would be close to the highest detected inter-ELM fluctuation frequencies (c.f. figure 4b). Since the QH-mode at ASDEX Upgrade is usually achieved at low pedestal top densities and collisionality, the E_r wells in the pedestal are consequently deep and the background E $\times$ B rotation is high. This is in line with the fact that the detected frequencies of the high frequency fluctuations depend on the background velocity. However, a low frequency fluctuation corresponding to an EHO is not visible in the magnetic signals during the presence of the inter-ELM high frequency fluctuations.

Linear MHD stability analysis has shown that DIII-D QH-mode plasmas are situated in the current-driven region of the stability diagram close to the peeling-ballooning stability boundary, suggesting, the EHO to be caused by a saturated peeling mode [46]. For the high frequency magnetic fluctuations presented here the measured amplitude at the HFS is comparable to that at the LFS. This could be explained by peeling drive, which is HFS/LFS symmetric.

In summary, in the final phase of the ELM cycle a saturated mode is observed in the steep gradient region of the pedestal. It is associated with a saturation of the maximum pressure gradient well before an ELM onset. Over a wide variation of pedestal pressure gradients and different pedestal top pressures (c.f. figure 4b), the toroidal mode numbers at high frequency are in the range of 10 to 12. At the same time, modes with lower frequencies and n numbers between 2 and 6 can also be observed. Future investigations will concentrate on the detection of possible mode coupling between these modes.

6. Acknowledgement

The authors would like to thank C. Angioni for his input to the discussion on the interpretation of the results.

F. M. Laggner is a fellow of the Friedrich Schiedel Foundation for Energy Technology.

This work has been carried out within the framework of the EUROfusion Consortium and has received funding from the Euratom research and training programme 2014-2018 under grant agreement No 633053. The views and opinions expressed herein do not necessarily reflect those of the European Commission.

References

[1] Wagner F 2007 *Plasma Physics and Controlled Fusion* **49** B1–B33 URL http://dx.doi.org/10.1088/0741-3335/49/12b/S01

[2] Ryter F, Angioni C, Beurskens M, Cirant S, Hoang G T, Hogeweij G M D, Imbeaux F, Jacchia A, Mantica P, Suttrop W and Tardini G 2001 *Plasma Physics and Controlled Fusion* **43** A323–A338 URL http://dx.doi.org/10.1088/0741-3335/43/12a/325

[3] Zohm H 1996 *Plasma Physics and Controlled Fusion* **38** 105–128 URL http://dx.doi.org/10.1088/0741-3335/38/2/001

[4] Loarte A, Saibene G, Sartori R, Becoulet M, Horton L, Eich T, Herrmann A, Laux M, Matthews G, Jachmich S, Asakura N, Chankin A, Leonard A, Porter G, Federici G, Shimada M, Sugihara M and Janeschitz G 2003 *Journal of Nuclear Materials* **313** 962–966 URL http://dx.doi.org/10.1016/S0022-3115(02)01398-3

[5] Connor J W 1998 *Plasma Physics and Controlled Fusion* **40** 531–542 URL http://dx.doi.org/10.1088/0741-3335/40/5/002

[6] Snyder P B, Wilson H R, Ferron J R, Lao L L, Leonard A W, Osborne T H, Turnbull A D, Mossessian D, Murakami M and Xu X Q 2002 *Physics of Plasmas* **9** 2037–2043 URL http://dx.doi.org/10.1063/1.1449463

[7] Snyder P B, Groebner R J, Hughes J W, Osborne T H, Beurskens M, Leonard A W, Wilson H R and Xu X Q 2011 *Nuclear Fusion* **51** 103016 URL http://dx.doi.org/10.1088/0029-5515/51/10/103016

[8] Dickinson D, Saarelma S, Scannell R, Kirk A, Roach C M and Wilson H R 2011 *Plasma Physics and Controlled Fusion* **53** 115010 URL http://dx.doi.org/10.1088/0741-3335/53/11/115010

[9] Dickinson D, Roach C M, Saarelma S, Scannell R, Kirk A and Wilson H R 2013 *Plasma Physics and Controlled Fusion* **55** 074006 URL http://dx.doi.org/10.1088/0741-3335/55/7/074006

[10] Saarelma S, Beurskens M N A, Dickinson D, Frassinetti L, Leyland M J, Roach C M and EFDA-JET Contributors 2013 *Nuclear Fusion* **53** URL http://dx.doi.org/10.1088/0029-5515/53/12/123012

[11] Told D, Jenko F, Xanthopoulos P, Horton L D, Wolfrum E and the ASDEX Upgrade Team 2008 *Physics of Plasmas* **15** 102306 URL http://dx.doi.org/10.1063/1.3000132

[12] Doerk H, Jenko F, Gorler T, Told D, Pueschel M J and Hatch D R 2012 *Physics of Plasmas* **19** 055907 URL http://dx.doi.org/10.1063/1.3694663

[13] Manz P, Boom J E, Wolfrum E, Birkenmeier G, Classen I G J, Luhmann N C, Stroth U and the ASDEX Upgrade Team 2014 *Plasma Physics and Controlled Fusion* **56** 035010 URL http://dx.doi.org/10.1088/0741-3335/56/3/035010

[14] Dickinson D, Roach C M, Saarelma S, Scannell R, Kirk A and Wilson H R 2012 *Physical Review Letters* **108** 135002 URL http://dx.doi.org/10.1103/PhysRevLett.108.135002

[15] Hatch D, Told D, Jenko F, Doerk H, Dunne M, Wolfrum E, Viezzer E, the ASDEX Upgrade Team and Pueschel M 2015 *Nuclear Fusion* **55** 063028 URL http://dx.doi.org/10.1088/0029-5515/55/6/063028

[16] Burckhart A, Wolfrum E, Fischer R, Lackner K, Zohm H and the ASDEX Upgrade Team 2010 *Plasma Physics and Controlled Fusion* **52** 105010 URL http://dx.doi.org/10.1088/0741-3335/52/10/105010

[17] Bolzonella T, Zohm H, Maraschek M, Martines E, Saarelma S, Gunter S and the ASDEX Upgrade Team 2004 *Plasma Physics and Controlled Fusion* **46** A143–A149 URL http://dx.doi.org/10.1088/0741-3335/46/5a/015

[18] Diallo A, Hughes J W, Greenwald M, Labombard B, Davis E, Baek S G, Theiler C, Snyder P, Canik J, Walk J, Golfinopoulos T, Terry J, Churchill M, Hubbard A, Porkolab M, Delgado-Aparicio L, Reinke M L, White A and the Alcator C-Mod Team 2014 *Phys Rev Lett* **112** 115001 URL http://dx.doi.org/10.1103/PhysRevLett.112.115001

[19] Diallo A, Hughes J, Baek S G, LaBombard B, Terry J, Cziegler I, Hubbard A, Davis E, Walk J, Delgado-Aparicio L, Reinke M, Theiler C, Churchill R, Edlund E, Canik J, Snyder P, Greenwald M, White A and the Alcator C-Mod Team 2015 *Nuclear Fusion* **55** 053003 URL http://dx.doi.org/10.1088/0029-5515/55/5/053003

[20] Diallo A, Groebner R J, Rhodes T L, Battaglia D J, Smith D R, Osborne T H, Canik J M, Guttenfelder W and Snyder P B 2015 *Physics of Plasmas* **22** 056111 URL http://dx.doi.org/10.1063/1.4921148

[21] Fischer R, Fuchs C J, Kurzan B, Suttrop W, Wolfrum E and the ASDEX Upgrade Team 2010

Fusion Science and Technology **58** 675–684
[22] Wolfrum E, Aumayr F, Wutte D, Winter H P, Hintz E, Rusbuldt D and Schorn R P 1993 *Review of Scientific Instruments* **64** 2285–2292 URL http://dx.doi.org/10.1063/1.1144460
[23] Fischer R, Wolfrum E, Schweinzer J and the ASDEX Upgrade Team 2008 *Plasma Physics and Controlled Fusion* **50** 085009 URL http://dx.doi.org/10.1088/0741-3335/50/8/085009
[24] Willensdorfer M, Birkenmeier G, Fischer R, Laggner F M, Wolfrum E, Veres G, Aumayr F, Carralero D, Guimarais L, Kurzan B and the ASDEX Upgrade Team 2014 *Plasma Physics and Controlled Fusion* **56** 025008 URL http://dx.doi.org/10.1088/0741-3335/56/2/025008
[25] Mlynek A, Reich M, Giannone L, Treutterer W, Behler K, Blank H, Buhler A, Cole R, Eixenberger H, Fischer R, Lohs A, Luddecke K, Merkel R, Neu G, Ryter F, Zasche D and the ASDEX Upgrade Team 2011 *Nuclear Fusion* **51** 043002 URL http://dx.doi.org/10.1088/0029-5515/51/4/043002
[26] Suttrop W 1997 *IPP Report* 1–28
[27] Rathgeber S K, Barrera L, Eich T, Fischer R, Nold B, Suttrop W, Willensdorfer M, Wolfrum E and the ASDEX Upgrade Team 2013 *Plasma Physics and Controlled Fusion* **55** 025004 URL http://dx.doi.org/10.1088/0741-3335/55/2/025004
[28] Kurzan B, Murmann H, Salzmann H and the ASDEX Upgrade Team 2001 *Review of Scientific Instruments* **72** 1111–1114 URL http://dx.doi.org/10.1063/1.1321747
[29] Neuhauser J, Coster D, Fahrbach H U, Fuchs J C, Haas G, Herrmann A, Horton L, Jakobi M, Kallenbach A, Laux M, Kim J W, Kurzan B, Muller H W, Murmann H, Neu R, Rohde V, Sandmann W, Suttrop W, Wolfrum E and the ASDEX Upgrade Team 2002 *Plasma Physics and Controlled Fusion* **44** 855–869 URL http://dx.doi.org/10.1088/0741-3335/44/6/316
[30] Wolfrum E, Viezzer E, Burckhart A, Dunne M G, Schneider P A, Willensdorfer M, Fable E, Fischer R, Hatch D, Jenko F, Kurzan B, Manz P, Rathgeber S K and the ASDEX Upgrade Team 2015 *Nuclear Fusion* **55** 053017 URL http://dx.doi.org/10.1088/0029-5515/55/5/053017
[31] Sauter O, Angioni C and Lin-Liu Y R 1999 *Physics of Plasmas* **6** 2834–2839 URL http://dx.doi.org/10.1063/1.873240
[32] Willensdorfer M, Wolfrum E, Fischer R, Schweinzer J, Sertoli M, Sieglin B, Veres G, Aumayr F and the ASDEX Upgrade Team 2012 *Rev Sci Instrum* **83** 023501 URL http://dx.doi.org/10.1063/1.3682003
[33] Ida K and Hidekuma S 1990 *Physical Review Letters* **65** 1364–1367 URL http://dx.doi.org/10.1103/PhysRevLett.65.1364
[34] Viezzer E, Pütterich T, Angioni C, Bergmann A, Dux R, Fable E, McDermott R M, Stroth U, Wolfrum E and the ASDEX Upgrade Team 2014 *Nuclear Fusion* **54** 012003 URL http://dx.doi.org/10.1088/0029-5515/54/1/012003
[35] Viezzer E, Pütterich T, Conway G D, Dux R, Happel T, Fuchs J C, McDermott R M, Ryter F, Sieglin B, Suttrop W, Willensdorfer M, Wolfrum E and the ASDEX Upgrade Team 2013 *Nuclear Fusion* **53** 053005 URL http://dx.doi.org/10.1088/0029-5515/53/5/053005
[36] Viezzer E, Pütterich T, McDermott R M, Conway G D, Cavedon M, Dunne M G, Dux R, Wolfrum E and the ASDEX Upgrade Team 2014 *Plasma Physics and Controlled Fusion* **56** 075018 URL http://dx.doi.org/10.1088/0741-3335/56/7/075018
[37] Zohm H 2014 *Magnetohydrodynamic Stability of Tokamaks* (Weinheim: Wiley-VCH) ISBN 3527412328
[38] Horváth L, Poloskei P Z, Papp G, Maraschek M, Schuhbeck K, Pokol G I, the EUROfusion MST1 Team and the ASDEX Upgrade Team 2015 *Plasma Physics and Controlled Fusion* **57** 125005 URL http://dx.doi.org/10.1088/0741-3335/57/12/125005
[39] Perez von Thun C P, Maraschek M, da Graa S, Buttery R J, Herrmann A, Stober J, Conway G, Eich T, Fuchs J C, Horton L D, Igochine V, Kallenbach A, Loarte A, Mller H W, Nunes I, Saibene G, Sartori R, Sips A C C, Suttrop W and Wolfrum E 2008 *Plasma Physics and Controlled Fusion* **50** 065018 URL http://dx.doi.org/10.1088/0741-3335/50/6/065018
[40] Scott B D 2002 *New Journal of Physics* **4** 52 URL http://dx.doi.org/10.1088/1367-2630/4/

1/352

[41] Scott B D 2003 *Plasma Physics and Controlled Fusion* **45** A385 URL http://dx.doi.org/10.1088/0741-3335/45/12A/025

[42] Burrell K H, Austin M E, Brennan D P, DeBoo J C, Doyle E J, Fenzi C, Fuchs C, Gohil P, Greenfield C M, Groebner R J, Lao L L, Luce T C, Makowski M A, McKee G R, Moyer R A, Petty C C, Porkolab M, Rettig C L, Rhodes T L, Rost J C, Stallard B W, Strait E J, Synakowski E J, Wade M R, Watkins J G and West W P 2001 *Physics of Plasmas* **8** 2153–2162 URL http://dx.doi.org/10.1063/1.1355981

[43] Greenwald M, Boivin R, Bonoli P, Budny R, Fiore C, Goetz J, Granetz R, Hubbard A, Hutchinson I, Irby J, LaBombard B, Lin Y, Lipschultz B, Marmar E, Mazurenko A, Mossessian D, Pedersen T S, Pitcher C S, Porkolab M, Rice J, Rowan W, Snipes J, Schilling G, Takase Y, Terry J, Wolfe S, Weaver J, Welch B and Wukitch S 1999 *Physics of Plasmas* **6** 1943 URL http://dx.doi.org/10.1063/1.873451

[44] Suttrop W, Maraschek M, Conway G D, Fahrbach H U, Haas G, Horton L D, Kurki-Suonio T, Lasnier C J, Leonard A W, Maggi C F, Meister H, Muck A, Neu R, Nunes I, Pütterich T, Reich M, Sips A C C and the ASDEX Upgrade Team 2003 *Plasma Physics and Controlled Fusion* **45** 1399–1416 URL http://dx.doi.org/10.1088/0741-3335/45/8/302

[45] Suttrop W, Hynnen V, Kurki-Suonio T, Lang P T, Maraschek M, Neu R, Stbler A, Conway G D, Hacquin S, Kempenaars M, Lomas P J, Nave M F F, Pitts R A, Zastrow K D, the ASDEX Upgrade team and contributors to the JET-EFDA workprogramme 2005 *Nuclear Fusion* **45** 721–730 URL http://dx.doi.org/10.1088/0029-5515/45/7/021

[46] Snyder P B, Burrell K H, Wilson H R, Chu M S, Fenstermacher M E, Leonard A W, Moyer R A, Osborne T H, Umansky M, West W P and Xu X Q 2007 *Nuclear Fusion* **47** 961–968 URL http://dx.doi.org/10.1088/0029-5515/47/8/030